Something something something physics

Steven Green
of Emmanuel College

A dissertation submitted to the University of Cambridge
for the degree of Doctor of Philosophy

Abstract

This thesis describes the optimisation of the calorimeter design for collider experiments at the future Compact LInear Collider (CLIC) and the International Linear Collider (ILC). The detector design of these experiments is built around high-granularity Particle Flow Calorimetry that, in contrast to traditional calorimetry, uses the energy measurements for charged particles from the tracking detectors. This can only be realised if calorimetric energy deposits from charged particles can be separated from those of neutral particles. This is made possible with fine granularity calorimeters and sophisticated pattern recognition software, which is provided by the PandoraPFA algorithm. This thesis presents results on Particle Flow calorimetry performance for a number of detector configurations. To obtain these results a new calibration procedure was developed and applied to the detector simulation and reconstruction to ensure optimal performance was achieved for each detector configuration considered.

This thesis also describes the development of a software compensation technique that vastly improves the intrinsic energy resolution of a Particle Flow Calorimetry detector. This technique is implemented within the PandoraPFA framework and demonstrates the gains that can be made by fully exploiting the information provided by the fine granularity calorimeters envisaged at a future linear collider.

A study of the sensitivity of the CLIC experiment to anomalous gauge couplings that effect vector boson scattering processes is presented. These anomalous couplings provide insight into possible beyond standard model physics. This study, which utilises the excellent jet energy resolution from Particle Flow Calorimetry, was performed at centre-of-mass energies of 1.4 TeV and 3 TeV with integrated lumi-

nosities of 1.5ab^{-1} and 2ab^{-1} respectively. The precision achievable at CLIC is shown to be approximately one to two orders of magnitude better than that currently offered by the LHC.

Finally, a study into various technology options for the CLIC vertex detector is described.

Declaration

This dissertation is the result of my own work, except where explicit reference is made to the work of others, and has not been submitted for another qualification to this or any other university. This dissertation does not exceed the word limit for the respective Degree Committee.

Andy Buckley

Acknowledgements

Of the many people who deserve thanks, some are particularly prominent, such as my supervisor…

Preface

This thesis describes my research on various aspects of the LHCb particle physics program, centred around the LHCb detector and LHC accelerator at CERN in Geneva.

For this example, I'll just mention Chapter **??** and Chapter **??**.

Contents

"Writing in English is the most ingenious torture ever devised for sins committed in previous lives."

— James Joyce

Chapter 1

Reconstruction Chain

"There, sir! that is the perfection of vessels!"
— Jules Verne, 1828–1905

1.1 Reconstruction Chain

1.2 Event Generation, Simulation and Reconstruction

The jet fragmentation and hadronisation for the Z $\rightarrow$ uds events used for determining the metric for detector performance was controlled using PYTHIA [16] that had been tuned using data from LEP [6]. Single particle spatially isotropic samples of K_L^0, γ and μ^- were produced for the calibration of each detector model. A simple c++ script was written to generate the relevant HEPEvt common blocks for these samples.

Detector model simulation was performed using MOKKA [14], a GEANT4 [5] wrapper providing detailed geometric descriptions of detector concepts for the linear collider. Event reconstruction was performed using MARLIN [10], a c++ framework designed for reconstruction at the linear collider. PandoraPFA [13, 17] was used to apply Particle Flow Calorimetry in the reconstruction, the full details of which can be found in chapter PANDORA CHAPTER.

Chapter 2

Calorimeter Optimisation Studies

"The simple believes everything, but the prudent gives thought to his steps."
— Proverbs 14:15

2.1 Calorimeter Optimisation Studies

The fundamental principle of particle flow calorimetry is to measure the energy of a particle passing through a detector in whichever sub-detector offers the best energy resolution. For particle colliders experiments, this involves measuring the momenta of charged particles using the curvature of the track they create in the detector. This offers extremely good energy resolution in comparison to calorimetric energy measurements and is the source of the excellent energy resolution particle flow calorimetry can produce. As neutral particles produce no tracks, their energies must be measured using calorimetric energy deposits.

The application of particle flow calorimetry is extremely challenging as it is possible, by using incorrect associations of charged particle tracks to calorimetric energy deposits, to both double count and omit energy measurements. For example, if a charged particle calorimetric energy deposit is not associated to a track that energy deposit will be double counted, while if a neutral particle calorimetric energy deposit is associated to a track that energy deposit will be neglected. Therefore, making the correct associations between charged particle tracks and calorimetric energy deposits is essential.

These associations can only be successfully made if the calorimeters in use have fine segmentation, such as those found at the linear collider experiment, so that it becomes possible to separate the energy deposits from nearby showering particles. Even with this segmentation making the association of charged particle tracks to the calorimetric energy deposits is highly non-trivial. At the linear collider experiment, these associations are made using sophisticated pattern recognition algorithms, provided by PandoraPFA. The fine segmentation of the calorimeters allows PandoraPFA to reconstruct the four-momenta of all particles passing through the detector and to use the energy measurement from the optimal sub-detector in each case.

In this chapter optimisation of the calorimeters used at the linear collider, with focus placed on obtaining the best energy resolution for jets, is considered. Parameters such as the number of layers, cell size and material choices for the calorimeters are considered.

This chapter concludes with an optimisation of several global parameters for the detector such as the magnetic field strength used for the detector and the inner radius of the ECal. These parameters are not calorimeter specific, but affect the jet energy resolution obtained from particle flow.

2.2 Jet Energy Resolution

As many physics processes of interest at the linear collider involve multi-jet final states, good jet energy resolution is a crucial a aspect of detector performance. As shown in chapter PHYSICS ANALYSIS, parameters derived from the energy measurements of jets, such as invariant mass, are extremely useful for identification of physics channels of interest as well as determining the sensitivity of the linear collider experiments to areas of new physics. Therefore, the primary metric used in this study is the jet energy resolution.

Jet energy resolution in particular can benefit from the application of particle flow calorimetry as $\approx 70\%$ of the energy of jets are carried in the from of charged particles. As particle flow aims to measure the energy of charged particles using the tracker, it has the potential to offers extremely large benefits when measuring jet energies in comparison to the traditional calorimetric approach.

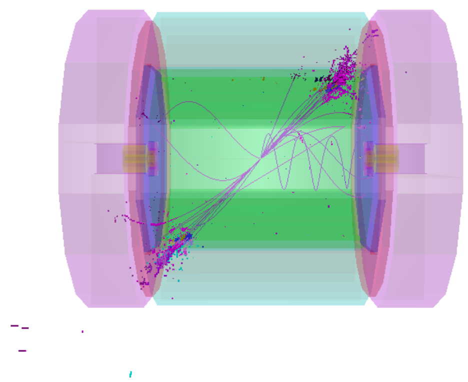

Figure 2.1: 500 GeV di-jet Z→uds event display for nominal ILD detector.

2.2.1 Jet Energy Resolution Metrics

The primary metric used to optimise detector performance is the jet energy resolution. This was found through the simulation of off-shell mass Z boson events decaying to light quarks (u, d, s). In these events the Z boson is produced at rest, which means the typical decays form two mono-energetic jets that are produced back to back as shown in figure 2.1. Only events where $|\cos(\theta)| < 0.7$, where θ is the polar angle of the quarks from the Z decay, are used in the metric calculation to ensure little energy is lost down the beam axis. Using these events the jet energy resolution is calculated as follows:

$$\frac{\mathrm{RMS}_{90}(E_i)}{\mathrm{Mean}_{90}(E_i)} = \frac{\mathrm{RMS}_{90}(E_{jj})}{\mathrm{Mean}_{90}(E_{jj})} \times \sqrt{2}, \tag{2.1}$$

where $\mathrm{RMS}_{90}(E_{jj})$ and $\mathrm{Mean}_{90}(E_{jj})$ are the root mean squared (RMS) and the mean of the reconstructed energy distribution calculated within the range of with the smallest RMS containing at least 90% of the data. respectively.

This definition is used to remove the effect of outliers in the distribution [17]. Although the correct combination of charged particle tracks and calorimetric energy measurements would give a Gaussian reconstructed jet energy distribution, the effect of confusion on certain events will distort this distribution and broaden the tails significantly. If the full range were to be used in the jet energy resolution calculation, the effect of these tails is overinflated. If the distribution of reconstructed jet energies

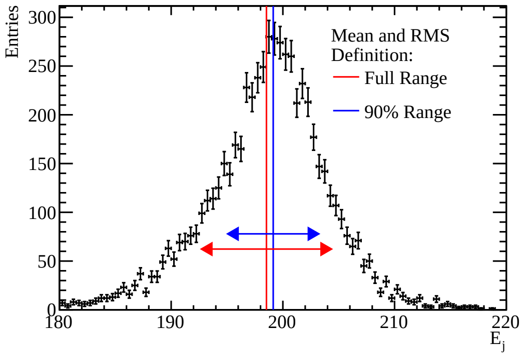

Figure 2.2: Definition of jet energy resolution. Reconstructed jet energy for 200 GeV di-jet Z→uds events for nominal ILD detector.

is truncated to the narrowest range of the data containing at least 90% of the data, the effect of these tails can be negated. This removes events where confusion is dominant, which makes the jet energy resolution metric far more robust and representative of the bulk of the data.

An example of the application of this metric can be found in figure 2.2. The RMS calculated using the full range 5.8 GeV, while the RMS using the reduced range is 4.1 GeV. This corresponds to a reduction in the jet energy resolution from 4.1% to 2.9%, which clearly shows an overemphasis of the tails of the distribution if the full range is used in the calculation.

In the subsequent analysis a range of di-jet energies were considered ranging from the Z mass, 91 GeV, to the nominal running energy of the ILC, 500 GeV. Each event sample contained 10,000 events generated spatially isotropically so that, given the polar angle cut, approximately 7,000 events contribute to the jet energy resolution metric.

2.2.2 Jet Energy Resolution Decompositions

The pattern recognition performed for the linear collider experiments is full described in section PANDORA SECTION, however, it is possible to gain further insight into the detector performance by cheating various parts of the pattern recognition using the MC information. Pattern recognition confusion manifests itself on energy measurements in two ways:

- If part of the calorimetric energy deposit from a charged particle is not associated to the track that energy deposit is double counted.
- If part of the calorimetric energy deposit from a neutral particle is incorrectly associated to a track, the energy deposit is not accounted for.

Both of these sources of confusion lead to inaccurate measurements of the jet energy and thus degrade the resolution. Cheating the pattern recognition, therefore, removes the effects of confusion and improves the detector performance.

The intrinsic energy resolution contribution to the jet energy resolution was determined by fully cheating the pattern recognition; in this case all confusion is negated. The total confusion is defined as the quadrature difference between the jet energy resolution using the standard reconstruction and this fully cheated reconstruction. Furthermore, it is possible to cheat the pattern recognition associated with individual types of particles. This is particularly useful for studies related to the ECal as, by cheating the photon pattern recognition, it is possible to isolate the confusion associated with photons. The photon confusion is defined as the quadrature difference between the jet energy resolution using the standard reconstruction and the reconstruction where photons pattern recognition is cheated.

2.2.3 Single Particle Energy Resolution

Several physics studies rely on the identification of single particles, such as γ in anomalous triple gauge coupling studies CITE, and as such the energy resolution of individual particles is presented alongside the jet energy resolution metric. As only uncharged particle energies are measured in the calorimeters in the particle flow paradigm, the single particle energy resolution is shown using γs and for K_L^0s. γs are particularly relevant for several physics studies and, as they are largely contained within the ECal, they provide insight into detector changes related purely to the ECal. This makes γs a natural choice of particle to consider for this study. K_L^0s were used as, analogously to γs and the ECal, their energies are primarily measured using the HCal. Although in general neutral hadron energy resolutions are less crucial to physics studies, the energy resolution is still a crucial contribution to the jet energy resolution, which should not be overlooked. For these single particle samples the energy resolution is defined using a Gaussian fit to the reconstructed energy distributions. The fit was applied to the narrowest region of the reconstructed

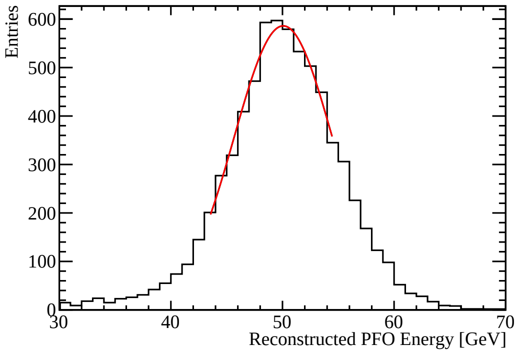

(a) 50 GeV K_L^0.

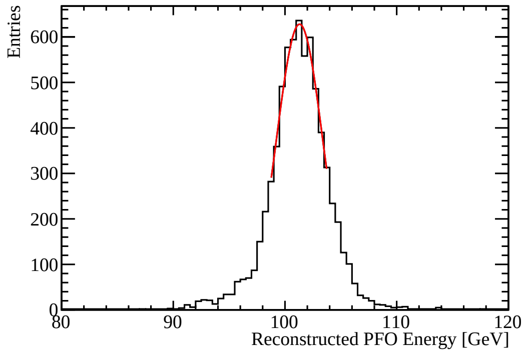

(b) 100 GeV γ.

Figure 2.3: The reconstructed energy distribution for (a) 50 GeV K_L^0 and (b) 100 GeV γ events. The red line shows a Gaussian fit used to parameterise the detector performance. The fit was applied to the truncated range of the reconstructed PFO energy distribution containing at least 75% of the data with the narrowest RMS. The nominal ILD model was used in this simulation.

PFO energy distribution that contained at least 75% of the data. This increases the likelihood that the fit converges and ensures a better parameterisation of the bulk of the data set. The resolution is defined as the standard deviation divided by the mean of that reconstructed Gaussian. A total of 10,000 events are used to calculate the energy resolution at each fixed energy point. A cut of $|\cos(\theta)| < 0.7$ is applied to ensure events avoid the Barrel/EndCap overlap region. Examples of the single particle energy distributions for 100 GeV γs and 50 GeV K_L^0s alongside the Gaussian fit used to determine their energy resolution are shown in figure 2.3. The errors quoted on single particle energy resolutions are determined by propagating the errors reported from the Gaussian fit into the resolution calculation.

2.3 Nominal Detector Performance

Before addressing the optimisation of the detectors for use at a future linear collider is it necessary to properly quantify the behaviour of the nominal detector model that is used in the simulations. For these studies the nominal ILD model is used.

The calorimeters at a linear collider are sampling calorimeters, therefore, the reconstructed energy distributions for neutral particles whose energies are measured in the calorimeters will be Gaussian. This is expected due as the active material for each calorimeter cell essentially counts the number of charged particle tracks passing through it, or possible the number of photons for scintillator options. The working hypothesis for estimating the energy deposited in a sampling calorimeter is that the energy of a showering particle is proportional to the number of charged particle tracks, or photons for scintillator detector options, it produces. Having counted the number of tracks in the active region of the calorimeter cell it is possible to estimate the energy deposited in the whole calorimeter cell in the digitisation process, further details on this can be found in chapter CALIBRATION CHAPTER. Finally, the energy of the entire particle shower is estimated by grouping the calorimeter cells and summing their energy. Each calorimeter cell energy is an independently random measurements and, by the central limit theorem CITE, the sum of a large number of independently random measurements has a Gaussian distribution. It follows that the variance of the shower energy distribution is given by the sum of the variances for each of the calorimeter cell energy distributions.

As each calorimeter hit involves counting a number of objects, charged particle tracks or photons, the statistics governing the distribution of the individual cell energies are Poisson statistics. For a given particle shower, if the mean of a cell energy is given by $\lambda = N$ where N is the mean number of objects that are expected, the standard deviation of that distribution is $\sigma = \sqrt{\lambda} = \sqrt{N}$ and the energy resolution $\frac{\sigma}{\lambda} = \frac{1}{\sqrt{N}}$. As the total shower energy, E_{Reco}, is proportional to N_{Reco}, the total number of tracks recorded in the calorimeter, the energy resolution for an ideal calorimeter is proportional to $\frac{1}{\sqrt{N_{Reco}}} = \frac{1}{\sqrt{E_{Reco}}}$. This gives the form of the energy resolution as a function of energy for an ideal calorimeter as $\frac{\sigma_{Reco}}{E_{Reco}} = \frac{a}{\sqrt{E_{Reco}}}$. In reality, it is typical to express the energy resolution of a calorimeter in the following form

$$\frac{\sigma_{Reco}}{E_{Reco}} = \frac{a}{\sqrt{E_{Reco}}} \oplus b \oplus \frac{c}{E_{Reco}}, \tag{2.2}$$

where the b term is a constant term that accounts for a variety of effects such as CHECK and the c term accounts for electrical noise.

Prototypes of the various ILD calorimeter options have been constructed and validated using test beam. The energy resolution measured using the test beam was parameterised as $\frac{16.6}{\sqrt{E_{Reco}}} \oplus 1.1\%$ for the silicon ECal and $\frac{12.9}{\sqrt{E_{Reco}}} \oplus 1.2\%$ for the scintillator ECal [2]. The electrical noise was deemed sufficiently small that the c term in the parameterisation could be neglected in both cases. These results were determined using an e^- test beam with energies ranging up to $\approx$ 40 GeV. This parametrisation is compared to the results found using the full ILD detector simulation in figures 2.4a and 2.4b for the silicon and scintillator ECal options respectively. The parameterisation of the energy resolution for the silicon ECal option is almost identical to the energy resolution results when using the full ILD simulation. However, for the scintillator ECal option the parameterisation is significantly better than that observed in the full simulation. This difference is most likely due to an imperfect implementation of the scintillator ECal within the full detector simulation. Even with this difference, the γ energy resolutions measured using the full ILD simulation when using the silicon and scintillator ECal options are similar. At very high energies, $\approx$ 500 GeV, the ECal is no longer sufficient to fully contain the γs and so leakage into the HCal leads to a minor degradation the energy resolution for the full simulation. This accounts for the deviation in the energy resolution between the full ILD simulation and the test beam parameterisation for the silicon ECal option.

Similarly, the energy resolution using test beam was parameterised as $\frac{57.6}{\sqrt{E_{Reco}}} \oplus 1.6\%$ for the nominal ILD HCal [3]. A comparison between this test beam parameterisation and the full ILD simulation, using the silicon ECal option, is shown in figure 2.4c. The test beam used for this parameterisation used $\pi^{\pm}$s with energies ranging from 10 to 80 GeV. In the determination of the test beam parameterisation, only showers starting in the HCal were considered whereas all showers were considered in the full ILD simulation. Negating showers starting in the ECal removes the effect of errors associated with the calibration of ECal for hadronic energy measurements and leads to a better energy resolution for the K_L^0. The deviation between the test beam parameterisation and the full simulation grows at high K_L^0 energies due to the treatment of energy deposits leaking out of the back of the HCal. A tail catcher was used in the test beam analysis that had a similar structure to the HCal, but with a much wider average absorber thickness. Energy deposits in this tail catcher were calibrated in a similar fashion to the HCal giving a very good energy resolution for these energy deposits. In the full ILD simulation a muon chamber acts as the tail catcher, however, the calibration applied to energy deposits here is far less advanced than that applied to the test beam data meaning the energy resolution for these hits will be worse. Furthermore, energy deposits in the uninstrumented solenoid region of the full ILD simulation are not accounted for. These lost energy deposits and simplistic calibration are the main causes of the deviation of the test beam parameterisation and the full simulation energy resolution for high energy K_L^0s.

Combining these results together it is possible to demonstrate the effectiveness of particle flow calorimetry on the jet energy resolutions. After the decay of short lived particles approximately 60% of the energy of a jet is carried in the form of charged particles, 30% in the form of γs and 10% in the form of neutral hadrons. A negligible amount of energy is also carried in the form of invisible energy i.e. neutrinos. In the traditional calorimetric approach the γs are measured largely within the ECal, with an energy resolution of $\approx 0.15 \times \sqrt{E_\gamma}$, and the remaining particles are measured in the HCal, with an energy resolution of $\approx 0.55 \times \sqrt{E_h}$. Note here that these are the raw, not fractional energy resolutions. Therefore, the contributions to the fractional jet energy resolution are $\frac{0.08}{\sqrt{E_j}}$ from γs and $\frac{0.46}{\sqrt{E_j}}$ from other particles where E_j is the jet energy. These add in quadrature to give a total jet energy resolution of $\frac{0.47}{\sqrt{E_j}}$. In the particle flow paradigm the energy of charged particles is measured in the tracker, which has such a good energy resolution than the contribution to the jet energy resolution is negligible. This means the contributions to the jet energy resolutions only come from γs, $\frac{0.08}{\sqrt{E_j}}$, and from neutral hadrons, $\frac{0.17}{\sqrt{E_j}}$. When added in quadrature they give a total jet energy resolution of $\frac{0.19}{\sqrt{E_j}}$, which is significantly better than when using the traditional calorimetric approach. It must be emphasised that this is an upper limit on the performance as the effect of confusion will degrade the jet energy resolution. However, by applying sophisticated pattern recognition algorithms this confusion can be minimised and exceptional performance achieved.

The jet energy resolutions as a function of jet energy using the full ILD simulation are shown in figure 2.4d. Alongside this the intrinsic energy resolution and confusion contributions to the jet energy resolution are also presented. For low jet energies the jet energy resolution is dominated by the intrinsic energy resolution of the detector. This indicates that the charged particle track to calorimeter hit cluster associations being made are largely correct and that the resolution is being driven by the energy resolution of the calorimeters. For high jet energies the event topology is more dense and mote error are present in the track cluster associations being made. Even at these large energies, the intrinsic energy resolution of the detector, which goes as $\frac{1}{\sqrt{E_j}}$, has reduced so much that the performance at high energies is better than that observed for the low energies. When the performance is put into context, these jet energy resolutions are sufficiently low, $\frac{\sigma_E}{E} \lesssim 3.8\%$ [2, 12, 17], that it is possible to separate

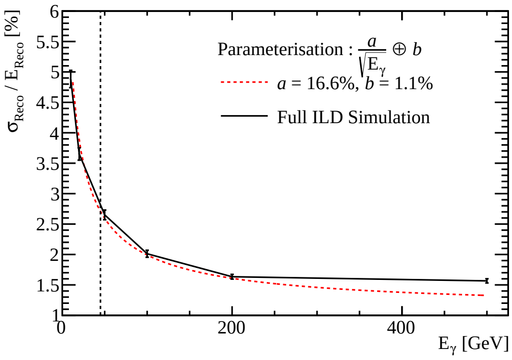

(a)

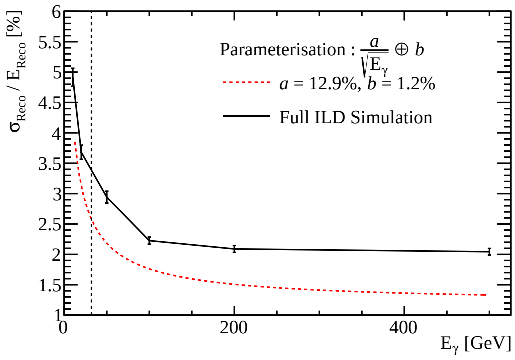

(b)

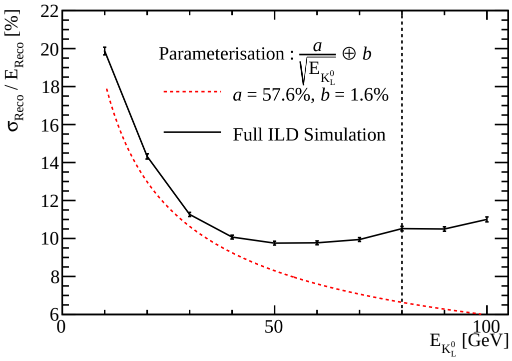

(c)

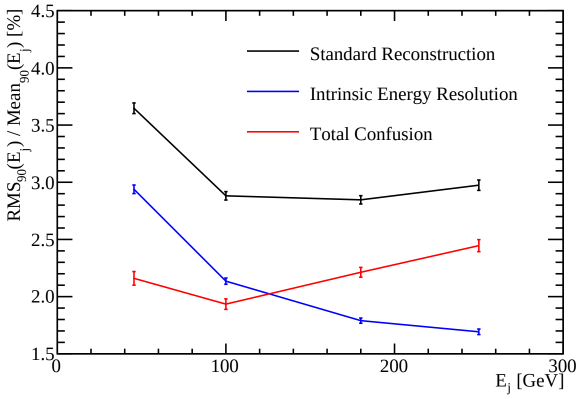

(d)

Figure 2.4: (a) The energy resolution as a function of γ energy using the nominal ILD model for the silicon ECal option. (b) The energy resolution as a function of γ energy using the nominal ILD model for the scintillator ECal option. (c) The energy resolution as a function of K_L^0 energy using the nominal ILD model with the silicon ECal option. (d) The jet energy resolution (RMS_{90}) as a function of jet energy using the nominal ILD model with the silicon ECal option. The intrinsic energy resolution and confusion contributions these the jet energy resolutions are also presented. The black dotted line on the single particle energy resolutions shows the highest energy particles used in the test beam measurements.

hadronic W and Z decays, which is one of the key requirements for the future linear collider.

2.4 Electromagnetic Calorimeter Optimisation

The ECal primarily measures the energy deposits of electromagnetic showers. The ECal in the nominal ILD detector model, summarised in table 2.1, is a silicon-tungsten sampling calorimeter. It contains 24 radiation lengths (X_0), which is sufficient to contain all but the highest energy electromagnetic showers, and has 29 readout layers. The absorber thickness of the last nine layers is twice that of the first 20 layers to reduces the number of readout channels and cost of the overall calorimeter while retaining a high sampling rate. This high sampling rate is crucial for the pattern recognition aspect of particle flow calorimetry, especially in the region where particle showers start developing, as shown in section 2.4.1.

Parameter	Default Value
Cell Size	$5 \times 5\text{mm}^2$ square cells
Number of Layers	29 readout layers
Active Material Choice	Silicon or Scintillator
Active Material Thickness	0.5 mm (Silicon) or 2 mm (Scintillator)
Absorber Material Choice	Tungsten
Absorber Material Thickness	20 layers of 2.1 mm followed by 9 layers of 4.2 mm

Table 2.1: The configuration of the ECal in the nominal ILD detector model. The parameters are given for the nominal silicon model as well as the alternative scintillator option.

The calorimeter performance was simulated for a number of detector models where the following detector parameters were varied:

- Cell size. This is a vital aspect of the detector in the particle flow paradigm as smaller cell sizes give greater potential for being able to separate energy deposits from charged and neutral particles. This should have little to no effect on the intrinsic energy resolution of the detector.
- Number of layers or sampling frequency. In this study the layer thicknesses are varied to keep the total number of radiation lengths within the detector constant. By increasing the number of layers in the calorimeter a particle shower is sampled more thoroughly leading to a reduction in the stochastic contribution to the energy resolution. Therefore, the number of layers will governs the intrinsic energy resolution of the calorimeter.

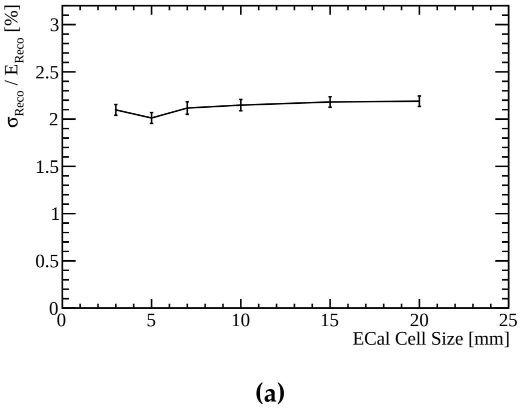

Figure 2.5: The energy resolution as a function of ECal cell size for 100 GeV γs using the nominal ILD detector model with (a) the silicon and (b) the scintillator ECal option.

- Active material choice, with the option of either silicon or scintillator as the active medium. As well as providing different intrinsic energy resolutions the readout mechanics of these two options are significantly different. There is no clear prior knowledge as to which should provide better performance.

2.4.1 ECal Cell Size

A number of different detector models were considered where the cell size in the ECal was varied about the nominal value of $5 \times 5\text{mm}^2$ square cells. The granularities considered were $3 \times 3\text{mm}^2$, $5 \times 5\text{mm}^2$, $7 \times 7\text{mm}^2$, $10 \times 10\text{mm}^2$, $15 \times 15\text{mm}^2$ and $20 \times 20\text{mm}^2$ square cells for both the silicon and scintillator active material options.

The energy resolution, using 100 GeV γ events, as a function of the ECal cell size is shown in figure 2.6a for the silicon option and figure 2.6b for the scintillator option. As at these energies the γ will be largely contained within the ECal these results relate solely to the energy resolution of the ECal within the full ILD simulation. For both the silicon and scintillator ECal options the energy resolution does not depend strongly on the ECal cell size. This is to be expected as the sampling frequency, which is the main factor in determining the energy resolution of a calorimeter, does not change when modifying the cell size. There are minor fluctuations in the energy resolution when varying the cell size, but these are mostly likely due to fluctuations in the energy response from calibration procedure that was applied to each detector models. For the scintillator ECal option there is a significant degradation in the energy resolution for the $3 \times 3\text{mm}^2$ cell size model. The most likely cause of this is a "dead" region in the active material, which represents the readout multi pixel photon counter (MPPC). The MPPC occupies a fixed area of the cell irrespective of cell size and so fractionally the dead region of the cell increases as cell size is reduced (CITE). The larger this dead region the worse the sampling of the electromagnetic showers in the ECal and the worse the resolution. While this effect will be present in all scintillator ECal options, it will only be significant for the small cell sizes when fractionally the dead region is largest. This would explain why the degradation is only seen at the smallest cell size considered.

The separation of nearby particle showers within the calorimeter is limited by the cell size. Smaller cell size make it easier separate nearby particle showers, which causes a reduction in the track to calorimeter cluster association confusion. Therefore, although the intrinsic energy resolution of a calorimeter is not dependent on the cell size it is expected that the jet energy resolution be far more sensitive to the ECal cell size. The jet energy resolution as a function of ECal cell size is shown in figure 2.6a for the silicon option and figure 2.6b for the scintillator option. As expected there is a very strong dependancy on the ECal cell size with smaller cell sizes leading to lower values of the jet energy resolution. The origin of this trend is best illustrated by considering the intrinsic energy resolution and confusion contributions to the jet energy resolution, which are shown as a function of ECal cell size for 45 and 250 GeV jets, for both the silicon and scintillator ECal options, in figure 2.7. It is clear from these contributions that the intrinsic energy resolution of the detector does not change when varying the cell size, which agrees with both prior expectations of calorimeter behaviour and the single particle energy resolution study. The minor fluctuations seen in the energy resolution for the single particle study are washed out when considering the intrinsic energy resolution for jets, as only 30% of jet energy is carried in the form of γs. Furthermore, the jet energy resolution trend as a function of the ECal cell size is being driven purely by changes to the confusion contribution and, in particular, the confusion caused by the reconstruction of γs. This is exactly what is to expected given the ECal primarily measures γs and shows that the performance of the ECal when varying the cell size is well understood.

It is clear that the ECal cell size is extremely important for the jet energy resolution of the detector, but it has little bearing on the intrinsic energy resolution. To ensure separation of hadronic decays of W and Z bosons is possible at ILC like energies an ECal cell size of least $15 \times 15\text{mm}^2$ is crucial, however, as reducing the ECal cell

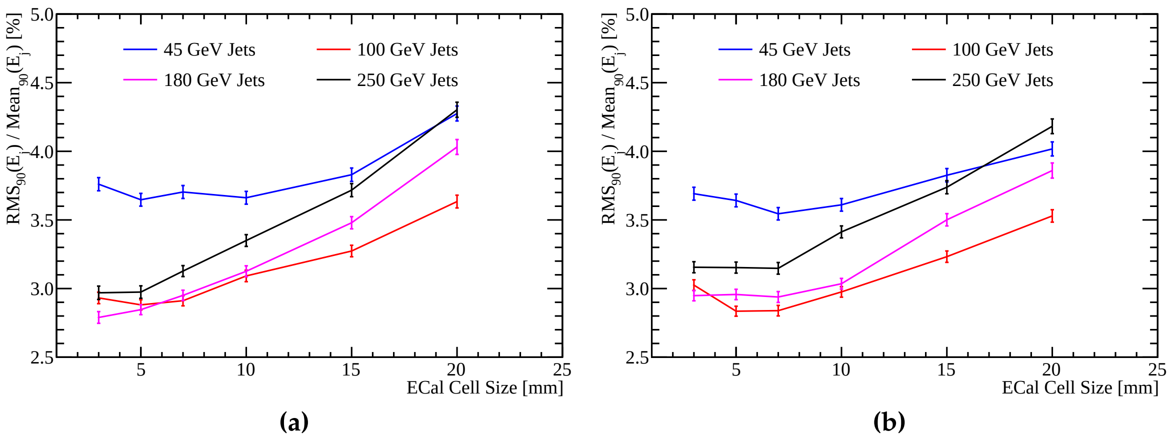

Figure 2.6: The jet energy resolution as a function of ECal cell size for various jet energies using the nominal ILD detector model with (a) the silicon and (b) the scintillator ECal option.

size further continues to improve the jet energy resolution choosing the smallest size possible is desirable.

2.4.2 ECal Number of Layers

The ECal performance was simulated for different numbers of sampling layers, while keeping the total material budget (X_0) approximately constant. This study was performed for both the silicon and scintillator active material options. In all cases tungsten was used for the ECal absorber material and the active layer thicknesses were not changed from those used in the nominal ECal models found in table 2.1. The different layouts for the ECals considered here are summarised in table 2.2.

The energy resolution, using 100 GeV γ events, as a function of the number of layers in the ECal is shown in figure 2.8a for the silicon option and figure 2.8b for the scintillator option. As the number of layers is reduced the energy resolution increases, which is expected as more layers means greater the sampling of the electromagnetic particle showers and a reduction in the stochastic contribution to the energy resolution. The trend observed for the scintillator option is less smooth than that observed for the silicon option. This will be due to the minor fluctuations appearing in the energy resolutions from the calibration of the simulation.

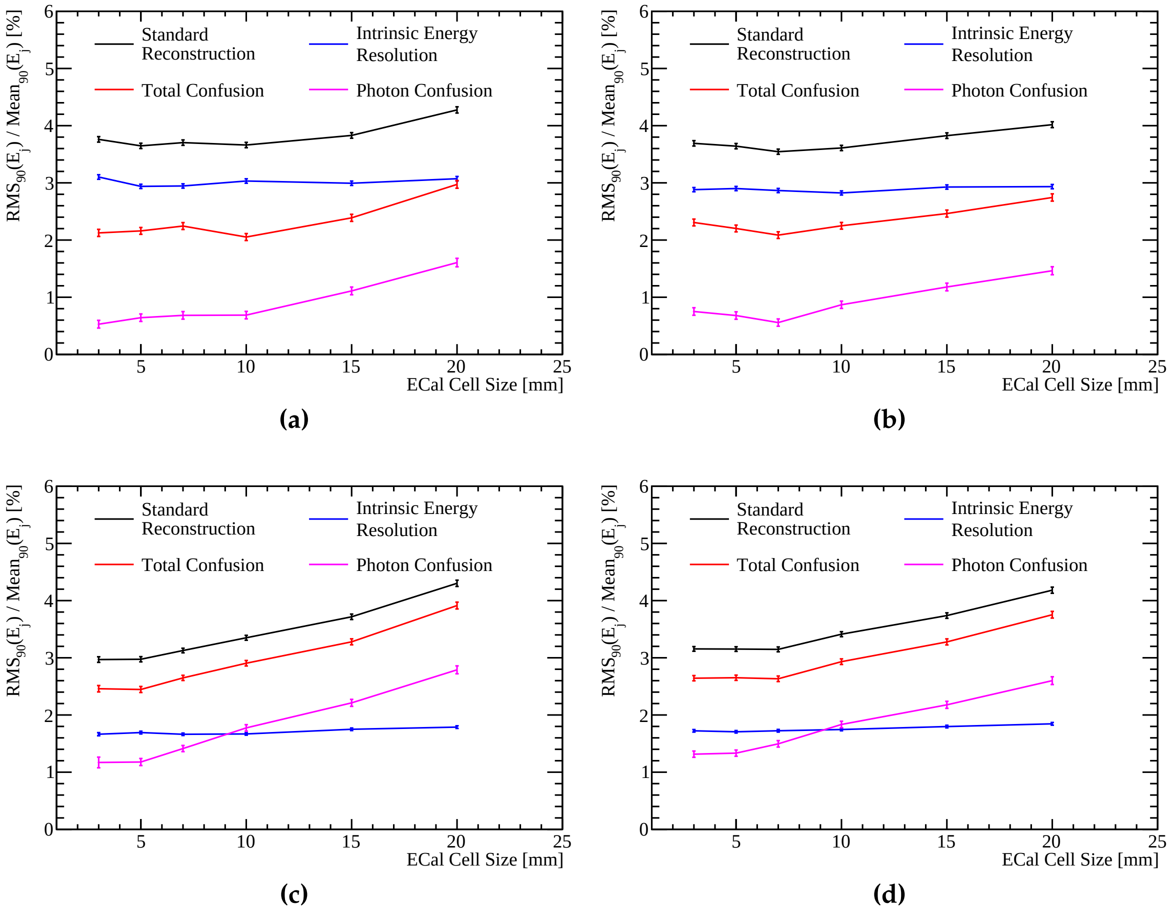

Figure 2.7: The contributions to the jet energy resolution as a function of ECal cell size using the nominal ILD detector model for (a) the silicon ECal option and 45 GeV jets, (b) the scintillator ECal option and 45 GeV jets, (c) the silicon ECal option and 250 GeV jets and (d) the scintillator ECal option and 250 GeV jets. The black curve correspond to the standard reconstruction, the blue curve to the intrinsic energy resolution contribution to the jet energy resolution, the red curve to the confusion contribution to the jet energy resolution and the magenta curve to the confusion contribution to the jet energy resolution related solely to γ reconstruction

Total Number of Layers $N_{\text{Layers ECal}}$	N_{Layers} Region 1	Absorber Thickness Region 1 [mm]	N_{Layers} Region 2	Absorber Thickness Region 2 [mm]	Total Thickness [X_0]
30	20	2.10	9	4.20	22.77
26	17	2.40	8	4.80	22.60
20	13	3.15	6	6.30	22.47
16	10	4.00	5	8.00	22.31

Table 2.2: The longitudinal structure of the ECal models considered in the optimisation study. The radiation length of tungsten absorber is 3.504mm [15]. Note that a presampler layer contributes one extra layer to the cumulative number of layers value for all detector models considered.

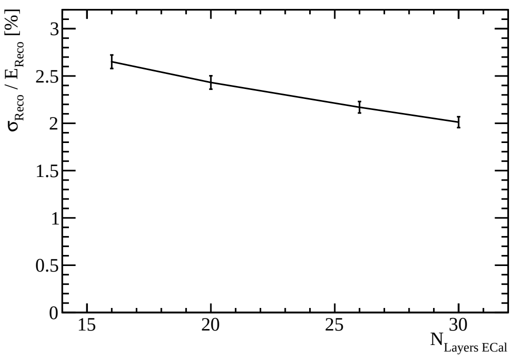

(a)

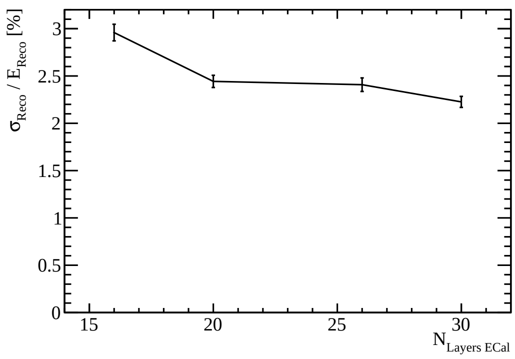

(b)

Figure 2.8: The energy resolution as a function of number of layers in the ECal for 100 GeV γs using the nominal ILD detector model with (a) the silicon and (b) the scintillator ECal option.

The confusion contribution to the jet energy resolution is lowered when the intrinsic energy resolution of the calorimeters improves. Improving the energy resolution of the ECal leads to more accurate the energy comparisons between the energy of clusters of calorimeter hits and the momentum of charged particle tracks leading to fewer calorimetric energy deposits where the energy is either double counted or not counted at all. When the number of layers in the ECal is increased the intrinsic energy resolution of the ECal improves, which has the knock on effect of reducing the confusion contribution to the jet energy resolution, which can be seen in figure 2.9a for the silicon ECal option and figure 2.9b scintillator ECal option. In both cases the jet energy resolution was found to improve when the number of layers in the

ECal is increased. The magnitude of the change in jet energy resolution was, however, dependent upon the jet energy, with a stronger dependancy being observed for low energy jets. The origin of this trend will be the stochastic term in the energy resolution for a sampling calorimeter, which is $\propto \frac{1}{\sqrt{E \times N_{Layers}}}$ where E is the reconstructed energy and N_{Layers} is the number of layers in the calorimeter. At high jet energies the energy resolution in the ECal is small and changes to the stochastic term that occur when varying the number of layers are too fine to be resolved using jet energy resolution. While at low jet energies the stochastic term is larger making it possible to resolve the changes to it when varying the number of layers in the ECal. The jet energy resolution is less sensitive then the single γ energy resolution to changes in the number of ECal layers as only $\approx 30\%$ of jet energy is carried in the form of γs. The decomposition of the jet energy resolution into the intrinsic energy resolution and confusion contributions for 45 and 250 GeV jets using both the silicon and scintillator ECal options are shown in figure 2.10. As expected, the twofold reduction in both the intrinsic energy resolution and the confusion contributions to the jet energy resolution is observed when increasing the number of layers in the ECal. Furthermore, changes to both jet energy resolution contributions when varying the number of layers in the ECal are comparable in size indicating that they are both crucial for determining the overall detector performance.

Increasing the number of layers in the ECal is beneficial to the intrinsic energy resolution of the ECal as well as the jet energy resolution, particularly for low jet energies. Separation of the W and Z hadronic decays should be possible for ILC like energies given there are at least 26 layers in the ECal, however, it is desirable to have as large a number of layers as possible to benefit single γ energy resolution also.

2.4.3 ECal Active Material

In sections 2.4.1 and 2.4.2 the performance of the ECal was reported for both the silicon and scintillator options and to a large extent the performance of the two options was the similar, but not identical:

- The intrinsic energy resolution of the silicon ECal option is better than that of a scintillator option for high energies, see figures 2.4a and 2.4b. This is most likely due to the implementation of Birks' law [7] for scintillator active materials. Birks'

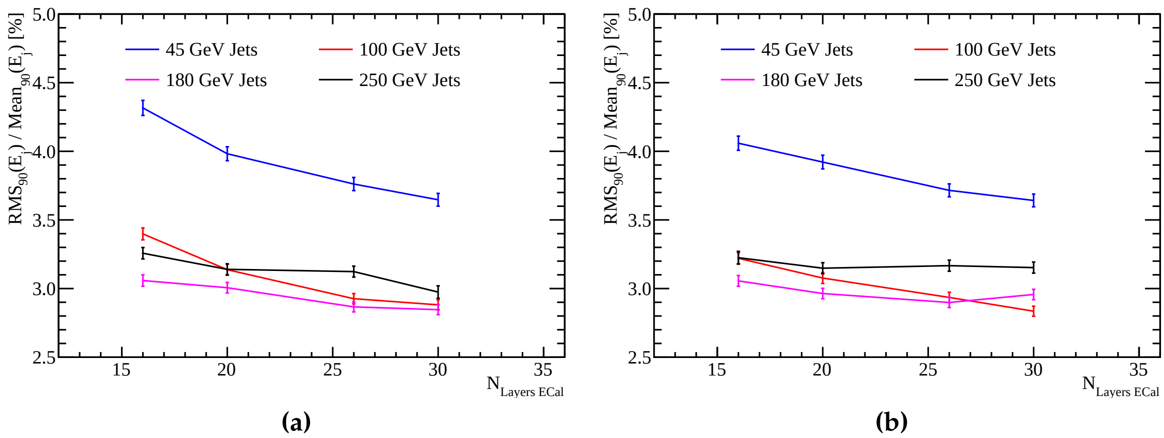

Figure 2.9: The jet energy resolution as a function of number of layers in the ECal for various jet energies using the nominal ILD detector model with (a) the silicon and (b) the scintillator ECal option.

law states:

$$\frac{d\mathcal{L}}{dx} \propto \times \frac{dE/dx}{1 + k_B dE/dx} \tag{2.3}$$

where $\frac{d\mathcal{L}}{dx}$ is the light yield per unit path length, dE/dx is the energy deposited per unit path length and k_B is a material property constant. For large energy deposits per unit length, such as those found in high energy γ events, the light yield saturates causing a degradation in the energy resolution. Based on a comparison with the silicon ECal option performance, this effect starts to degrade the energy resolution for the scintillator option around 50 GeV. However, the degradation in energy resolution up to 100 GeV is relatively small.

- The "dead" region due to the presence of the MPPC in the simulation of the scintillator ECal option degrades performance of the detector for small transverse granularities, see figure 2.5.

In summary, the performance of the two options in terms of energy and jet energy resolution are similar meaning no clear option is preferred. However, the silicon option is preferred when manufacture and implementation of the two models is compared. While constructing silicon wafers to fit the $5 \times 5\text{mm}^2$ square cell size of the ECal is achievable, this would be extremely challenging for scintillator tiles. To resolve this in reality the scintillator ECal option would have to use $5 \times 45\text{mm}^2$ scintillator strips that are arranged in alternating directions in each ECal layer. By combining information

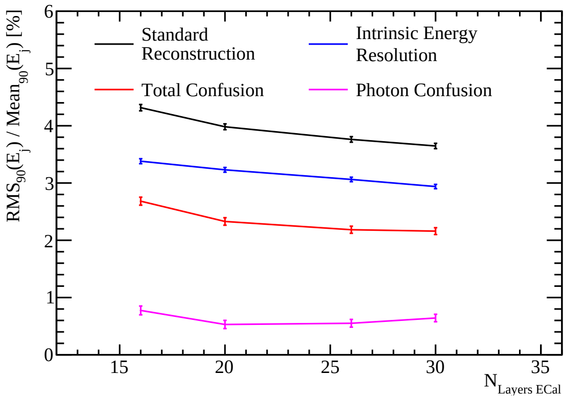

(a) Silicon active material, 45 GeV Jets.

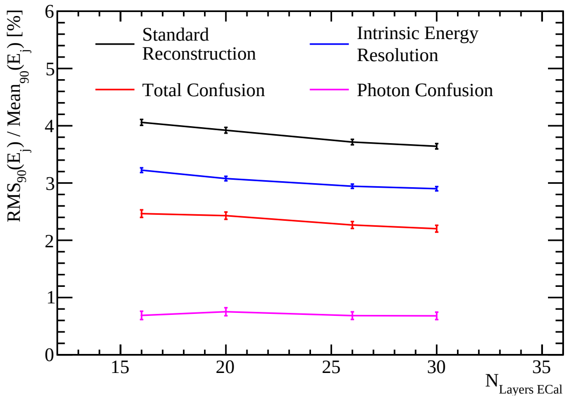

(b) Scintillator active material, 45 GeV Jets.

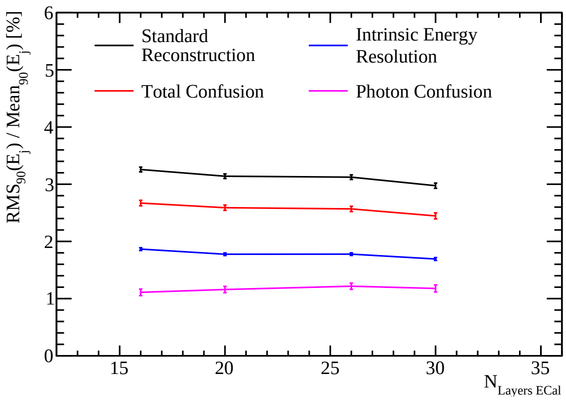

(c) Silicon active material, 250 GeV Jets.

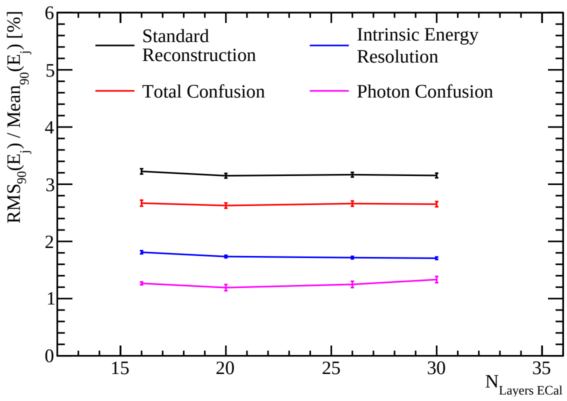

(d) Scintillator active material, 250 GeV Jets.

Figure 2.10: The contributions to the jet energy resolution as a function of number of layers in the ECal using the nominal ILD detector model for (a) the silicon ECal option and 45 GeV jets, (b) the scintillator ECal option and 45 GeV jets, (c) the silicon ECal option and 250 GeV jets and (d) the scintillator ECal option and 250 GeV jets. The black curve correspond to the standard reconstruction, the blue curve to the intrinsic energy resolution contribution to the jet energy resolution, the red curve to the confusion contribution to the jet energy resolution and the magenta curve to the confusion contribution to the jet energy resolution related solely to γ reconstruction.

from neighbouring layers it becomes possible to effectively achieve a $5 \times 5\text{mm}^2$ square cell size. This further challenges to the reconstruction means that the silicon option is the more preferred ECal model.

2.5 Hadronic Calorimeter Optimisation

The HCal primarily measures energy deposits from hadronic showers. The HCal in the default ILD detector model, summarised in table 2.3, and is approximately 6 nuclear interaction lengths (λ_I) deep. The ECal contributes approximately one λ_I giving a total of $\approx 7\lambda_I$, which is sufficient to confine the bulk of jets up to 1 TeV events. The longitudinal structure of this model consists of 48 readout layers each containing a 3 mm active layer of scintillator and a 20 mm absorber layer of iron.

There are several readout approaches under consideration for the HCal including fully analogue, fully digital and semi-digital. The analogue readout measures the energy within each HCal cell using a continuous spectrum of possible values, while the digital readout only produces a response if the energy deposited within a calorimeter cell is above a given threshold. The semi-digital approach mirrors that of the digital approach, but has three responses each with a different energy threshold. While the energy resolution for digital calorimeters is not as good as that of analogue calorimeters the advantage they have is that it is possible to construct smaller calorimeter cells using a digital readout. In traditional calorimetry, a digital readout would only lead to a worsening energy resolution, however, in the particle flow paradigm pattern recognition is as important, if not more important, than energy resolution. As the calorimeter cell size governs the confusion contribution to the jet energy resolution, it is envisaged that the use of a digital readout would involve a trade off where intrinsic energy resolution is sacrificed for a reduction in the pattern recognition confusion. In the following studies only the analogue HCal is considered.

The HCal performance for single hadrons and the overall jet energy resolution will depend on the details of the HCal design. A number of options were simulated where the following parameters were varied:

- Cell size. This is key to successful application of pattern recognition in the particle flow paradigm, but should not change the intrinsic energy resolution.

Parameter	Default Value
Cell Size	$30 \times 30\text{mm}^2$ square cells
Number of Layers	48 readout layers
Active Material Choice	Scintillator
Active Material Thickness	3 mm
Absorber Material Choice	Steel
Absorber Material Thickness	20 mm

Table 2.3: The configuration of the HCal in the nominal ILD detector model.

- Number of layers leaving the absorber and active layers thicknesses unchanged. This changes the total depth of the HCal and so will determine the effect of leakage of energy out of the back of the HCal.
- The sampling frequency. This study involves changing the number of readout layers in the HCal but modifying the thicknesses of the active and absorber layers thicknesses to keep the total number of nuclear interaction lengths constant. As this modifies the sampling of particle showers in the calorimeter it will effect the intrinsic energy resolution of this sampling calorimeter.
- Sampling fraction. This is the ratio of the active medium thickness to the absorber medium thickness. This controls how particle showers within the calorimeter are sampled.
- Absorber material choice. Two options have been considered: steel and tungsten. This choice dictates the growth and propagation of hadronic showers and so plays a crucial role in calorimetry.

2.5.1 HCal Cell Size

The HCal cell size is an important detector parameter in the application of particle flow calorimetry. Smaller HCal cell sizes will lead to a finer spatial resolution that can be used to better separate charged and neutral particle calorimetric energy deposits, however, this will also lead to an increase in the number of readout channels, which will raise the cost of the calorimeter. Therefore, it is highly desirable to achieve the optimal physics performance using the largest cell size possible. The nominal ILD

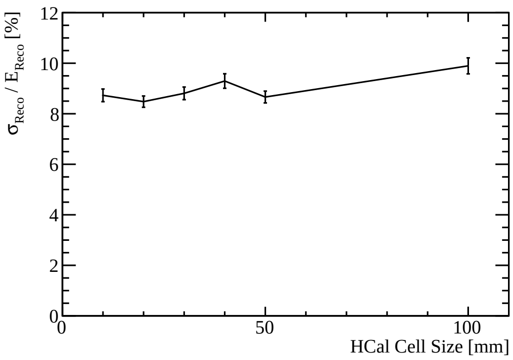

Figure 2.11: The energy resolution as a function of HCal cell size for 50 GeV K_L^0 events using the nominal ILD detector model.

HCal has a 30 mm square cell size and in this study the following square cell sizes were considered; 10 mm, 20 mm, 30 mm, 40 mm, 50 mm and 100 mm.

The energy resolution for 50 GeV K_L^0 events as a function of cell size in the HCal is shown in figure 2.11. These K_L^0 samples will deposit energy primarily within the HCal making them appropriate events to consider when determining the performance of the HCal, however, a non-neglibile amount of energy will also be deposited within the ECal. Therefore, these energy resolutions represents the intrinsic energy resolution of the ILD detector as a whole and not purely that of the HCal. It is clear that there is no strong dependency on the energy resolution of the K_L^0 as a function of the HCal cell size. There are small fluctuations in the energy resolution, but are most likely due to fluctuations from the calibration procedure and the precision in determining the optimal HCal cell truncation, described in section **??**. The precision of the optimal cell truncation is worse for large HCal cell sizes as the range of truncations considered for the optimisation is focused around the optimal truncation for the nominal ILD HCal truncation.

As a smaller HCal cell size will lead to better separation of charged and neutral hadron calorimetric energy deposits, it is expected that the confusion contribution to the jet energy resolution will be reduced by using smaller HCal cell sizes. The jet energy resolution as a function of cell size in the HCal shown in figure 2.12. At low jet energies there is no strong dependency of the jet energy resolution on the HCal cell size, which is as expected from the K_L^0 energy resolution study. For high energy jets there is a clear dependence, with lower HCal cell sizes leading to better jet energy resolutions. Examining the different contributions to the jet energy resolution,

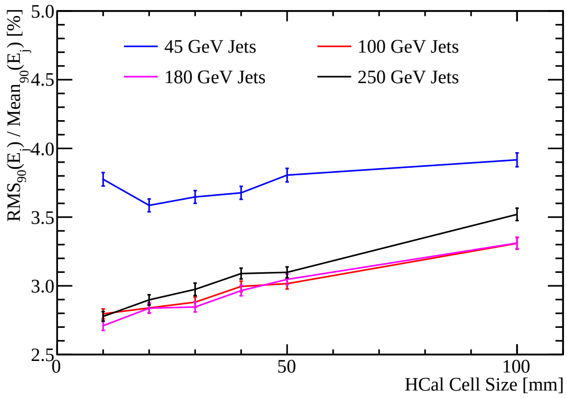

Figure 2.12: The jet energy resolution as a function of HCal cell size for various jet energies using the nominal ILD detector model.

shown in figure 2.13 it can be seen that the intrinsic energy resolution contribution is largely invariant to changes in the HCal cell size, modulo small fluctuations due to calibration, while the confusion contribution drives the overall trend in the jet energy resolution at high energies. The confusion contribution does fluctuate for small HCal cell sizes when considering low jet energies, but this will be due to tuning of the PandoraPFA algorithms to the nominal ILD HCal cell size. As the confusion contribution is not dominant at low energies, this effect is masked when considering the jet energy resolution metric. Furthermore, as the photon confusion is largely invariant to changes in the HCal cell size it indicates that the confusion contribution is changing due to pattern recognition improvements related to charged and neutral hadrons.

The jet energy resolution dependence on the HCal cell size is less strong than that observed in the ECal cell size, but that is to be expected as the ECal cell size determines the position of the start of showering particles in the calorimeters. If the start of a particle shower is well reconstructed in the ECal it becomes easier to associate the relevant calorimetric energy deposits in the HCal to it and vice verse. Therefore, a comparison of these studies indicates that ECal cell size is more crucial in the successful application of particle flow calorimetry than the HCal cell size is.

The confusion contribution to the jet energy resolution decreases by reducing the HCal cell size, while the intrinsic energy resolution of the detector is largely invariant to changes in the HCal cell size. As this dependancy is relatively weak such even using 100 mm square HCal cell sizes would be enough to allow for separation of the hadronic decays of W and Z bosons at ILC like energies. However, as jet energy

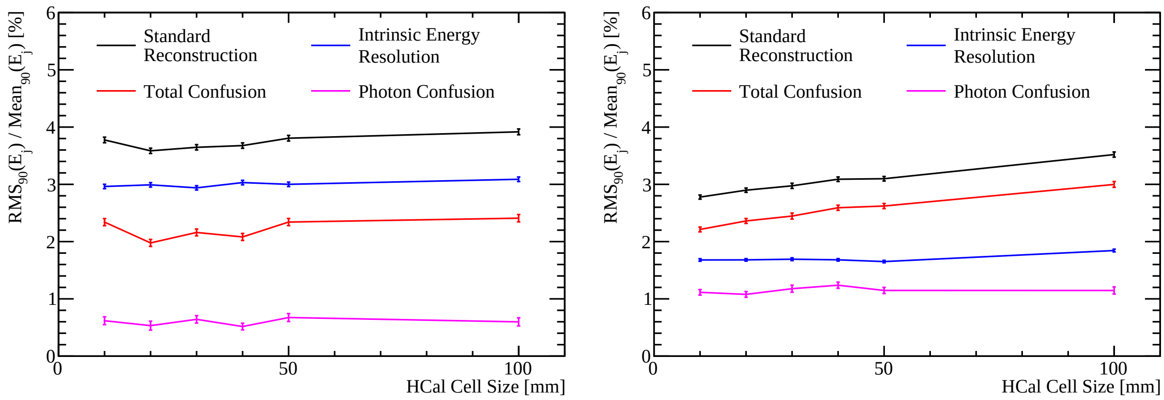

(a) 45 GeV Jets. **(b)** 250 GeV Jets.

Figure 2.13: The contributions to the jet energy resolution as a function of HCal cell size using the nominal ILD detector model for (a) 45 GeV jets and (b) 250 GeV jets. The black curve correspond to the standard reconstruction, the blue curve to the intrinsic energy resolution contribution to the jet energy resolution, the red curve to the confusion contribution to the jet energy resolution and the magenta curve to the confusion contribution to the jet energy resolution related solely to γ reconstruction.

resolution does improve with decreasing cell sizes it is desirable to have as small a HCal cell size as possible.

2.5.2 HCal Number of Layers

For this study the total number of layers in the HCal will be varied while leaving the active and absorber layer thicknesses unchanged. This means that the total thickness of the calorimeter is being modified, but the sampling frequency of particle showers within it does not. It is expected that this study will determine the effects of leakage of energy out of the back of the calorimeter, with a larger number of layers giving a smaller effect from leakage. As the cost of the HCal is proportional to the number of readout channels minimising the number of layers, while maintaining high quality physics performance is vital. For this study detector models were simulated with a HCal containing 36, 42, 48, 54 and 60 layers. The nominal ILD detector contains 48 layers.

It is expected that the energy resolution of the detector will improve with an increasing number of layers in the HCal up to a point as fewer events will suffer from the effects of leakage in a HCal with more layers. The improvement is only expected up

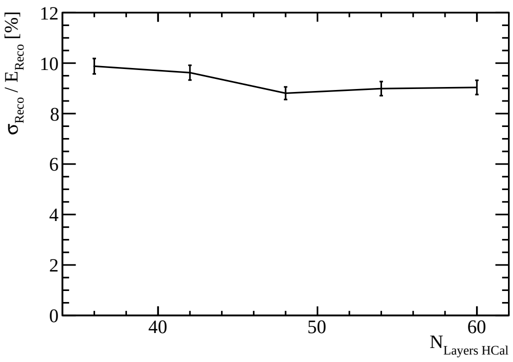

Figure 2.14: The energy resolution as a function of number of layers in the HCal for 50 GeV K_L^0 events using the nominal ILD detector model.

to a point as beyond this point almost all hadronic showers will be fully contained and so additional layers do not impact the energy measurements. The energy resolution as a function of number of layers in the HCal for 50 GeV K_L^0 is shown in figure 2.14. As expected the energy resolution degrades when the number layers is reduced below 48 layers, while above this additional layers do not yield better energy resolutions. However, even reducing the number of layers to 36 only causes a degradation in the energy resolution of the order of 1%.

The trend in the 50 GeV K_L^0 energy resolution when varying the number of layers in the HCal is unlikely to be seen in the jet energy resolution as it is a weak trend and only a small fraction of jet energy is measured within the HCal. However, the confusion contribution to the jet energy resolution is expected to change as, during the charged particle track to calorimeter cell cluster association, errors will be introduced if energy has leaked from the back of the calorimeter. For example, if a particle shower from a charged particle suffers heavily from leakage there will be a large disparity between the track momentum and the energy it deposits within the calorimeter. In that case, PandoraPFA will be overly aggressive in associating other calorimeter energy deposits to this track to account for the energy that has leaked out of the calorimeter, which will introduce errors. The jet energy resolution as a function of the number of layers in the HCal is shown in figure 2.15. As expected for low energy jets, where intrinsic energy resolution dominates, the jet energy resolution is invariant to the number of layers, while for high jet energies, where confusion dominates, a larger number of layers benefits the jet energy resolution. When examining the different contributions to the jet energy resolution, shown in figure **??**, it becomes clear that it is the confusion that drives the observed trends, while the intrinsic energy resolution is largely invariant to

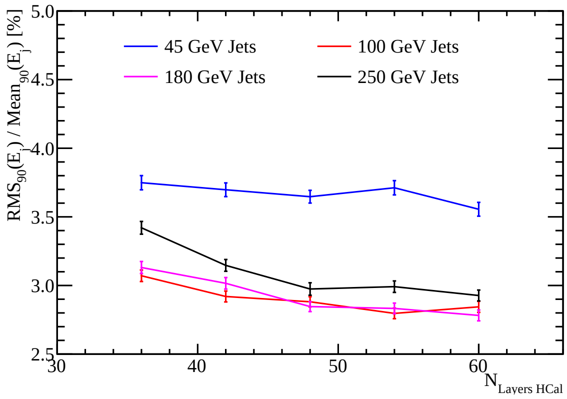

Figure 2.15: The jet energy resolution as a function of number of layers in the HCal for various jet energies using the nominal ILD detector model.

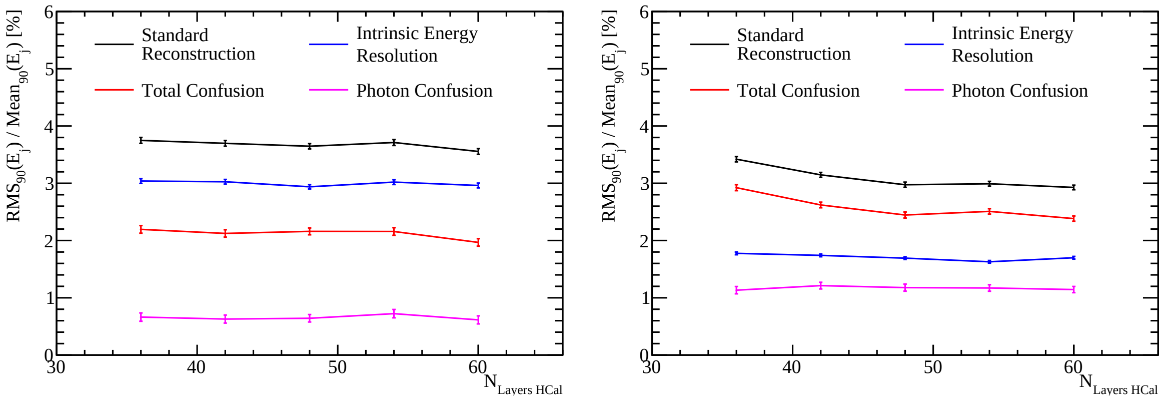

(a) 45 GeV Jets. **(b)** 250 GeV Jets.

Figure 2.16: The contributions to the jet energy resolution as a function of number of layers in the HCal using the nominal ILD detector model for (a) 45 GeV jets and (b) 250 GeV jets. The black curve correspond to the standard reconstruction, the blue curve to the intrinsic energy resolution contribution to the jet energy resolution, the red curve to the confusion contribution to the jet energy resolution and the magenta curve to the confusion contribution to the jet energy resolution related solely to γ reconstruction.

changes to the number of HCal layers as only a small fraction of jet energy is recorded in the HCal. Furthermore, the photon confusion is invariant to changes in the number of HCal layers, indicating that the change in the confusion contribution are originating from pattern recognition involving hadrons.

In summary, even if the number of layers in the HCal were reduced by a factor of 25% the jet energy resolution would be sufficient for separating the hadronic decays of the W and Z bosons at ILC energies. However, it is clear that leakage of energy from the back of the HCal would negatively affect events at ILC like energies should the number of layers be reduced from the nominal value of 48 layers, therefore it is desirable to have a minimum of 48 layers in the HCal.

2.5.3 HCal Sampling Frequency

In this study the sampling frequency in the HCal is examined. This is done by considering varying the number of readout layers in the HCal, while simultaneously varying the active and absorber layer thicknesses such that the total number of nuclear interaction lengths in the HCal is fixed. For each model considered the absorber material was steel, containing a total of 5.72 λ_I, while the active material was scintillator, containing a total of 0.19 λ_I. Furthermore, the ratio of the active to absorber layers thicknesses, the sampling fraction, was not changed. A summary of the detector models considered in this study can be found in table 2.4.

Number $N_{\text{Layers HCal}}$	Absorber Thickness [mm]	Active Thickness [mm]
60	16.00	2.40
54	17.78	2.67
48	20.00	3.00
42	22.86	3.43
36	26.67	4.00
30	32.00	4.80
24	40.00	6.00
18	53.33	8.00

Table 2.4: Cell size layout of various HCal models considered.

Increasing the number of layers in the HCal will increase the number of times a showering particle is sampled, which in turn will reduce the stochastic term in the energy resolution for a sampling calorimeter. Therefore, it is expected that the energy resolution will improve with increasing number of layers in the HCal. This is shown for 50 GeV K_L^0 in figure 2.17. Although there are fluctuations in the energy resolution, due to both fitting the Gaussian to extract the energy resolution and in the calibration of the detector, there is a clear trend showing that the energy resolution

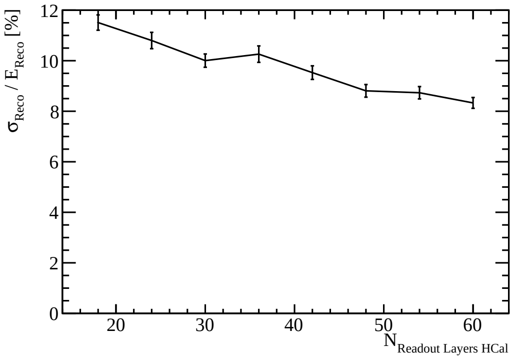

Figure 2.17: The energy resolution as a function of sampling frequency in the HCal for 50 GeV K_L^0 events using the nominal ILD detector model.

of the calorimeter is strongly dependent upon the sampling frequency in the HCal. The energy resolutions observed do not exactly follow a $\frac{1}{\sqrt{N_{\text{Readout Layers HCal}}}}$ relationship as these results are for the whole ILD detector, including the $\approx 1\lambda_I$ in the ECal, and not purely the HCal and this functional form neglects the constant term in the energy resolution.

As changing the sampling frequency of a calorimeter alters the intrinsic energy resolution, it is expected that this will produce a twofold effect on the jet energy resolution whereby the intrinsic energy improvements have the knock on effect of lowering confusion, as described in section 2.4.2 for changes to the number of layers in the ECal. The jet energy resolution as a function of sampling frequency in the HCal is shown in figure **??**. As expected there is an improvement in jet energy resolution at all energies due as both the intrinsic energy resolution and confusion are reduced with increasing sampling frequency, which can be seen when examining the different contributions to the jet energy resolution, shown in figure 2.19.

It is clear that a larger number of layers in the HCal benefits both the intrinsic energy resolution of the ILD detector as well as reducing the confusion contribution to the jet energy resolution. As there are few physics analyses that rely on the identification and categorisation of individual neutral hadrons, but there are many that rely on identification and categorisation of γs, the intrinsic energy resolution of the HCal is less crucial from a physics perspective than that of the ECal. However, these studies show the HCal still has a crucial role to play in jet reconstruction in the particle flow paradigm so cannot be neglected. To achieve a jet energy resolution of $\frac{\sigma_E}{E} \lesssim 3.8\%$, which is required to separate the W and Z hadronic decays, the ILD detector will

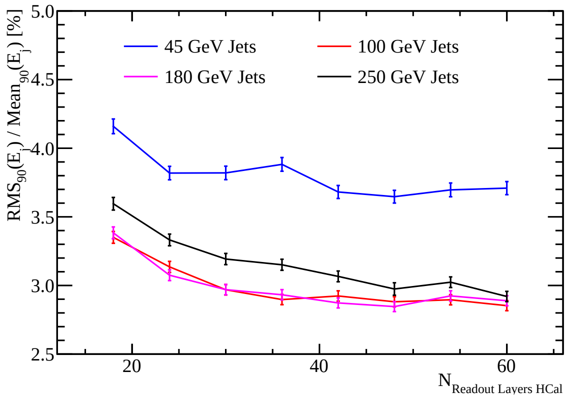

Figure 2.18: The jet energy resolution as a function of sampling frequency in the HCal for various jet energies using the nominal ILD detector model.

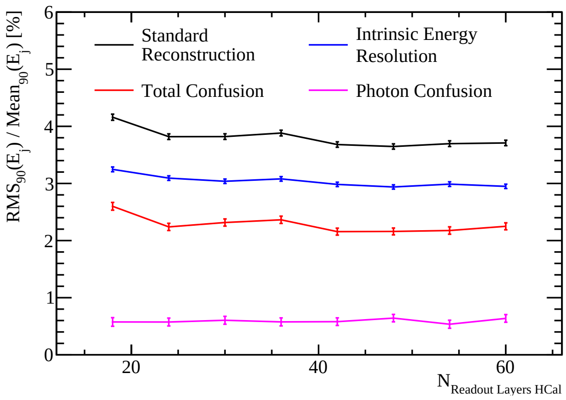

(a) 45 GeV Jets.

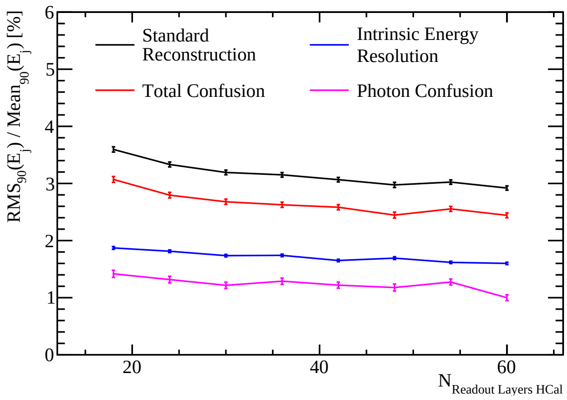

(b) 250 GeV Jets.

Figure 2.19: The contributions to the jet energy resolution as a function of sampling frequency in the HCal using the nominal ILD detector model for (a) 45 GeV jets and (b) 250 GeV jets. The black curve correspond to the standard reconstruction, the blue curve to the intrinsic energy resolution contribution to the jet energy resolution, the red curve to the confusion contribution to the jet energy resolution and the magenta curve to the confusion contribution to the jet energy resolution related solely to γ reconstruction.

require a minimum of 42 layers in the HCal. This sampling frequency is required in particular for lower energy jets where the energy resolution is dominated by the intrinsic energy resolution of the detector, while at higher energies the resolution is more than good enough to achieve the separation of the decay channels.

2.5.4 HCal Sampling Fraction

In this section the sampling fraction, the ratio of the active to absorber layer thicknesses were considered. For all detector models considered in this section the total number of nuclear interaction lengths in the HCal was held constant, as was the number of layers in the HCal and the cell size. The detector models considered are summarised in table 2.5.

Sampling Fraction	Absorber Thickness [mm]	Active Thickness [mm]
0.05	20.430	1.022
0.10	20.213	2.021
0.15	20.000	3.000
0.20	19.792	3.958
0.25	19.587	4.897

Table 2.5: Sampling fraction of HCal models considered.

The jet energy resolution for these detector models is shown in figure 2.18. It was found that there is no significant change in performance when varying the sampling fraction.

2.5.5 HCal Absorber Material

The nominal choice of absorber material is steel, tungsten provides a feasible alternative material. Although tungsten is more expensive than steel, it contains a larger number of nuclear interaction lengths per unit length. Therefore, using tungsten as opposed to steel as the absorber material would reduce the size of the HCal, while retaining the same number of nuclear interaction lengths. Reducing the depth of the

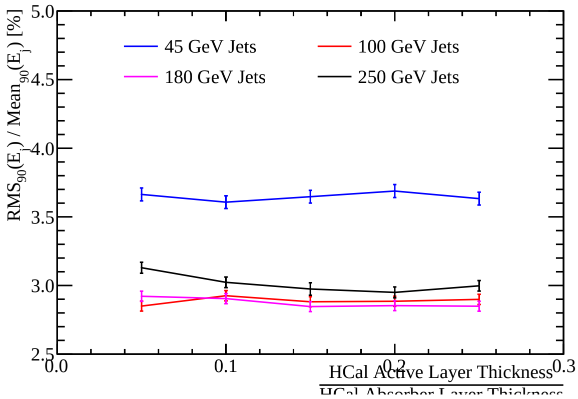

Figure 2.20: Jet energy resolution as a function of sampling frequency in the HCal. Label needs fixing.

calorimeter would decrease the size of the solenoid required, which would offset some of the additional cost if tungsten were used as the absorber material.

Parameter	Steel HCal Option	Tungsten HCal Option
Cell Size	$30 \times 30\text{mm}^2$ square cells	$30 \times 30\text{mm}^2$ square cells
Number of Layers	48 readout layers	48 readout layers
Absorber Material Thickness [mm]	20.0	12.0
Active Material Choice	Scintillator	Scintillator
Active Material Thickness [mm]	3.0	1.8

Table 2.6: The configuration of the stainless steel and tungsten HCal options.

The configuration for the stainless steel and tungsten HCal options that were used in the full ILD simulation can be found in table 2.6. To isolate the effects of changing the absorber material, the total depth, in nuclear interaction lengths, was kept constant when comparing these two options. Furthermore, the sampling fraction, the ratio of active to absorber layer thickness, was also held constants. The interaction of hadrons with the absorber material within the detector is simulated by GEANT4. A number of different physics lists exist within GEANT4 for the modelling of hadronic showers. The default model for high energy physics calorimetry is the QGSP_BERT physics list, which uses the quark-gluon string model [9] with the precompound model of nuclear evaporation [1] (QGSP) for high energy interactions and the Bertini (BERT) cascade model [11] for intermediate energy interactions. For this study both the QGSP_BERT and the QGSP_BERT_HP physics lists were used. The QGSP_BERT_HP list uses the high precision neutron package (NeutronHP) to deal with the transportation of neutrons from below 20 MeV to thermal energies. This added detail was thought to be necessary for a study involving tungsten due to the expected increase in shower development.

One of the dominant process governing the energy deposition of hadronic showers in calorimeters is spallation [18]. Spallation begins with the collision of a high energy incident particle with an atomic nuclei from the calorimeter absorbing material. This collision creates an internuclear cascade where a shower of high energy hadronic particles, e.g. protons, neutrons and pions, are produced within the nucleus. If these energies are large enough some of these particles may escape the nucleus and form secondary particles in the hadronic shower. After this initial collision the nuclei of the absorbing material are left in an excited state. Assuming the excited nuclei are sufficiently stable that they will not undergo fission, they will return to a stable state by ejecting energy in the form of particles in a process called evaporation. Evaporation of neutrons, which is the dominant form of evaporation, significantly delays the growth of hadronic showers as some of these neutrons undergo neutron capture [4]. Neutron capture involves an absorber nuclei capturing a neutron and then emitting a γ as it returns to a stable state. Therefore, the time it take for the neutron capture mechanism to proceed is limited by the lifetime of the unstable nuclei. This makes neutron capture one of the slowest mechanisms by which hadronic showers can propagate. As absorber materials with a large atomic number, Z, have a larger number of neutrons, it is expected that there will be an increase in the number of evaporation neutrons within hadronic showers developing in such materials. In turn this will lead to more neutron capture processes and a longer development time for the hadronic showers. This is what is observed when considering the shower development times using the tungsten (Z=74) and steel (iron, Z=26) HCal options as seen in figure 2.21.

HCal Option	Energy Resolution [%]
Stainless Steel, QGSP_BERT	8.8 ± 0.2
Stainless Steel, QGSP_BERT_HP	9.0 ± 0.3
Tungsten, QGSP_BERT	9.1 ± 0.2 Change this
Tungsten, QGSP_BERT_HP	9.0 ± 0.2 Change this

Table 2.7: The energy resolution using the nominal ILD detector with various HCal options determined using 50 GeV K_L^0 events.

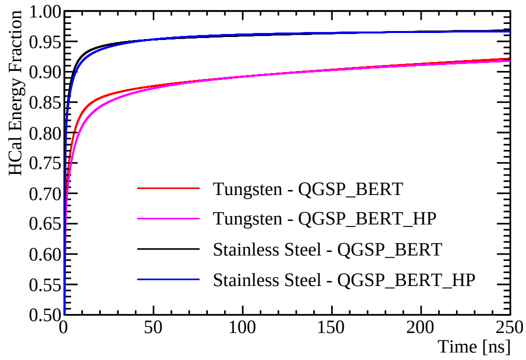

Figure 2.21: The fraction of the total calorimetric energy deposited in the HCal as a function of time for 25 GeV K_L^0 events using the steel and tungsten HCal options. Results are shown for both the QGSP_BERT and QGSP_BERT_HP physics lists. The calorimeter hit times have been corrected for straight line time of flight to the impact point.

The energy resolution for 50 GeV K_L^0 events using the nominal ILD detector model with a stainless steel and tungsten HCal absorber material can be found in table 2.7. No significant differences were seen in the energy resolution when changing the absorber material. Furthermore, the addition of the high precision neutron package did not alter the detector performance significantly.

HCal Option	Jet Energy Resolution [%]			
	45 GeV	100 GeV	180 GeV	250 GeV
Stainless Steel, QGSP_BERT	3.65 ± 0.05	2.88 ± 0.04	2.85 ± 0.04	2.97 ± 0.05
Stainless Steel, QGSP_BERT_HP	3.67 ± 0.05	2.92 ± 0.04	2.86 ± 0.04	3.03 ± 0.04
Tungsten, QGSP_BERT	3.78 ± 0.05	3.12 ± 0.04	3.15 ± 0.04	3.43 ± 0.04
Tungsten, QGSP_BERT_HP	3.80 ± 0.05	3.08 ± 0.04	3.24 ± 0.04	3.41 ± 0.04

Table 2.8: The jet energy resolution using the nominal ILD detector with various HCal options for various jet energies.

The jet energy resolutions for various jet energies are shown in table 2.8 for the various HCal options considered. These results indicate that steel outperforms tungsten as the absorber material for the HCal. Furthermore, as the jet energy increases the magnitude of the difference in jet energy resolutions between the two options increases. This indicates the differences in jet energy resolution between the two options is being driven by the confusion contribution to the jet energy resolution as contribution rises with increasing jet energy, while the intrinsic energy resolution contribution falls. Furthermore, as the K_L^0 energy resolution does not strongly depend on the HCal absorber material, it is expected that neither will the intrinsic energy resolution contribution to the jet energy resolution.

The intrinsic energy resolution and confusion contributions to the jet energy resolution for 45 and 250 GeV jets are shown in table 2.9. As expected the intrinsic energy resolution contribution to the jet energy resolution are nearly identical between the various options. It should be emphasised that this is only the case as the HCal cell truncation, as described in section **??**, was separately tuned for the tungsten option. This has to be modified as the average cell energy is greater when using tungsten, as opposed to steel, for the HCal absorber material. As the HCal primarily measures hadronic showers one may naively expect the number of radiation lengths in the HCal to be irrelevant to performance, given both options have the same number of nuclear interaction lengths, but this is not the case as all hadronic showers have an electromagnetic component, from the decays of $\pi^0 \rightarrow \gamma\gamma$. Therefore, these shower components deposit more energy per unit length in the HCal, which raises the average cell energy.

The confusion contribution to the jet energy resolution is larger for the tungsten HCal option than for the steel HCal option. This will be due to the PandoraPFA algorithms being tuned for HCal cell dimensions for the steel HCal option, while the cells for the tungsten option are thinner by a factor of approximately $\frac{\lambda_I^{Steel}}{\lambda_I^{Tungsten}} \approx 1.7$, where λ_I^x is the distance of one radiation length in material x. It is unfeasible to tune all of the PandoraPFA algorithms to each detector geometry, however, the breakdowns of the jet energy resolution indicate that even if it were possible to obtain the same confusion contributions for both options, the tungsten option would offer no advantage to the steel option in terms of the intrinsic energy resolution. Finally it was noted that the use of the QGSP_BERT_HP physics list, as opposed to QGSP_BERT, made a minimal impact on any of the results presented here.

In conclusion, there are no significant differences in the energy resolution when changing the HCal absorber material from steel to tungsten. The steel option HCal outperforms the tungsten option in terms of pattern recognition confusion, when

HCal Option	Jet Energy Resolution [%]			
	45 GeV		250 GeV	
	Intrinsic	Confusion	Intrinsic	Confusion
Stainless Steel, QGSP_BERT	2.93 ± 0.04	2.16 ± 0.06	1.69 ± 0.02	2.45 ± 0.05
Stainless Steel, QGSP_BERT_HP	2.98 ± 0.04	2.15 ± 0.06	1.65 ± 0.02	2.53 ± 0.04
Tungsten, QGSP_BERT	2.97 ± 0.04	2.34 ± 0.06	1.65 ± 0.02	3.01 ± 0.05
Tungsten, QGSP_BERT_HP	2.92 ± 0.04	2.42 ± 0.06	1.65 ± 0.02	2.99 ± 0.05

Table 2.9: The contributions to the jet energy resolution using the nominal ILD detector with various HCal options for 45 and 250 GeV jet energies.

using the default PandoraPFA settings, making it the more preferred option of the two.

2.6 Global Detector Parameters

This section focuses upon optimisation of two global detector parameters; the magnetic field strength and the ECal inner radius. While these are not directly related to the calorimeter they will both effect detector performance and so were deemed worthy of study alongside the calorimeter parameters.

2.6.1 The Magnetic Field Strength

The magnetic field is vital to the successful application of particle flow calorimetry. Any charged particles passing through the detector transverse helices that, once reconstructed, can be fitted to give the momentum and so energy of said particle in the particle flow paradigm. The magnetic field also created a separation between charged and neutral hadrons energy deposits in the calorimeters. The larger the magnetic field, the greater this separation and the easier to avoid confusion associate tracks to the correct energy deposits in the calorimeters, which is crucial for particle flow.

The magnetic field strengths considered in this study ranged from 1 to 5 T in steps of 0.5 T. The jet energy resolutions as a function of magnetic field strength, shown in

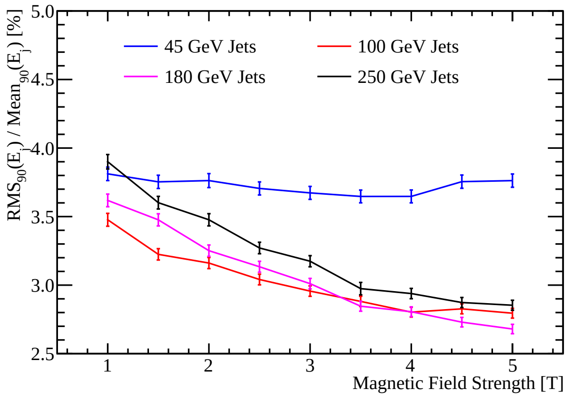

Figure 2.22: Jet energy resolution is shown for several fixed energy jets as a function of magnetic field strength.

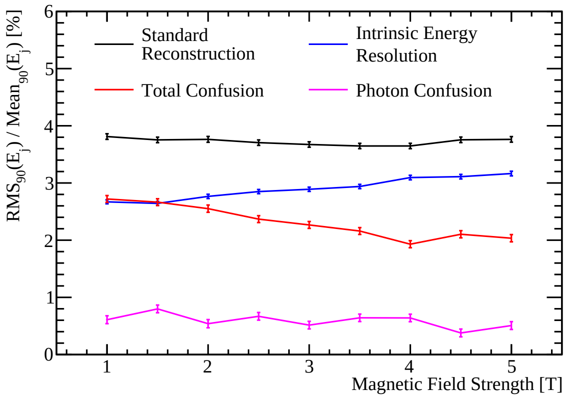

(a) 45 GeV Jets.

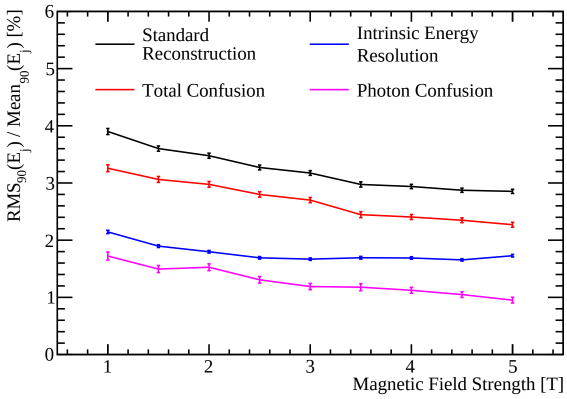

(b) 250 GeV Jets.

Figure 2.23: Jet energy resolution breakdown as a function of magnetic field strength for 45 and 250 GeV jets.

figure 2.22, shows that the jet energy resolution decreases with increasing magnetic field strength for high energy jets. At low energies the performance is largely invariant to magnetic field strength.

Examination of the decompositions of the jet energy resolution, found in figure 2.23, highlights a number of effects.

The first is a clear reduction in confusion with increasing magnetic field strength. This is due to a larger separation between charged and neutral hadron energy deposits in the calorimeter as was expected.

Secondly there is a reduction in intrinsic energy resolution with increasing magnetic field strength for low energy jets, while for high energy jets this trend is reversed.

At low energies the momenta of the charged particles will be low and so the radii of curvature of the helix these particles transverse will be small. If the radius for a given particle is small enough it will not make it into the calorimeters. In this case only if the track produced from this particle passes tight selection cuts designed to ensure the track originates from the impact point will the track be used to create a PFO. Therefor, energy can and will be lost in from events where PFOs are stuck within the tracker. Given the radii of curvature is inversely proportional to the magnetic field strength, the larger the magnetic field strength the more tracks will be confined to the tracker. The more tracks that are confined to the tracker, the worse the intrinsic energy resolution becomes as inevitably some tracks fail the quality cuts to form PFOs. At high jet energies the transverse momentum of the particles will be sufficiently large that the radii of curvatures of the helices formed by charged particles will be enough so that they reach the calorimeters on average. However, for low magnetic field strengths more particles deposit energy within the same calorimeter cells. The intrinsic energy resolution plot is determined by associating a single MC particle to each calorimeter cell. At high jet energies and low magnetic field strengths many of the cells will have energy deposits split between multiple cells and so associating a single MC particle per cell is inaccurate. This explains why the intrinsic energy resolution degrades slightly in this scenario. These results are still of interest, however, because the driving term in the jet energy resolution as a function of magnetic field strength is the confusion.

In summary, increasing the magnetic field strength is beneficial to detector performance as it reduces confusion from associating tracks to calorimetric energy deposits from charged particles. While there is a reduction in the intrinsic energy resolution for low transverse momentum jets with increasing magnetic field strength, this effect is largely offset by the change in confusion. While the nominal field of 3.5 T gives good performance increasing the field strength is a clear way of making large gains in detector performance.

2.6.2 Inner ECal Radius

This section focuses on optimising the inner ECal radius, or the outer tracker radius. The nominal detector model has an ECal inner radius of 1808 mm and for this optimisation detector models were considered where the ECal inner radii was set to 1208, 1408, 1608 and 2008 mm. All other detector parameters identical to those of the nominal ILD detector model.

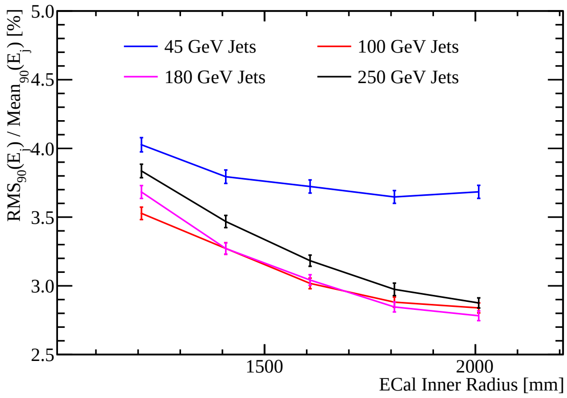

Figure 2.24: Jet energy resolution is shown for several fixed energy jets as a function of ECal inner radius.

The jet energy resolution as a function of ECal inner radius is shown in figure 2.24 and these results show that a large ECal inner radius was highly beneficial to detector performance. This is due to the fact that a large tracker gives more time for charged particles to bend due to the magnetic field, which creates a larger separation between calorimetric energy deposits from charged and neutral particles. This larger separation reduces the confusion when associating calorimetric energy deposits to tracks and so improves the detector performance. This conclusion is backed up by the decomposition of the jet energy resolution for the low and high energy jets, shown in figure **??**, which explicitly show a reduction in confusion with increasing ECal inner radius.

The intrinsic energy resolution of the detectors follows the same pattern as was observed in the magnetic field study. For low energy jets the larger ECal radius means fewer particles make it to the calorimeters and so some PFOs are not reconstructed giving a worse energy resolution. While at larger jet energies the radii of curvature of the charged particles is sufficiently large as the particles have higher momenta, meaning very few are confined to the tracker and so the intrinsic energy resolution is largely invariant. There is a small degradation in intrinsic energy resolution at low ECal inner radii due to the association of a single MC particle per calorimeter cell when running the cheated pattern recognition as explained in section 2.6.1. Again, this effect has little bearing on the final conclusions as the change in intrinsic energy resolution across the detector models is a second order effect.

In conclusion, increasing the ECal inner radius benefits the jet energy resolution significantly. This trend is driven by changes to the confusion in associating tracks to

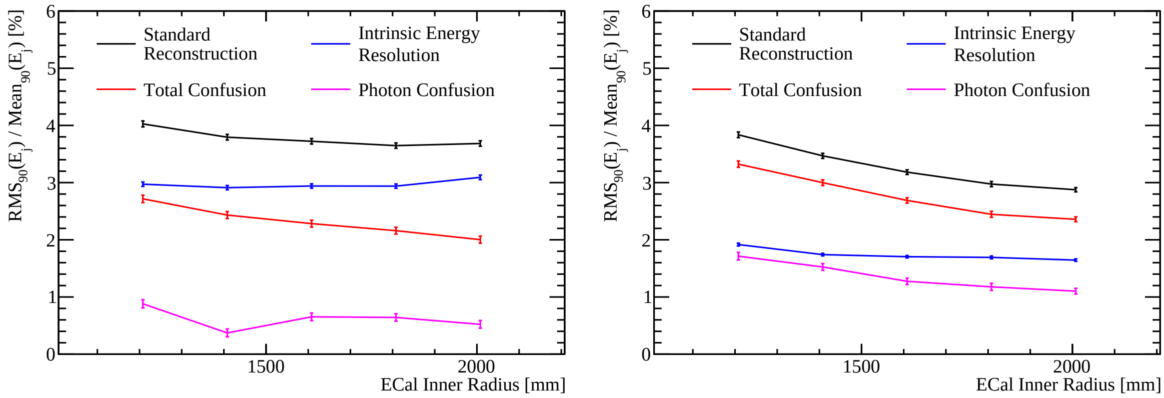

(a) 45 GeV Jets.

(b) 250 GeV Jets.

Figure 2.25: Jet energy resolution breakdown as a function of ECal inner radius for 45 and 250 GeV jets.

calorimetric energy deposits, with a larger ECal inner radius producing a reduction in the confusion as separation of charged and neutral particle energy deposits increases.

2.7 Conclusions

Colophon

This thesis was made in $\LaTeX\,2_\varepsilon$ using the "hepthesis" class [8].

Bibliography

[1] *Geant4 Physics Reference Manual, Section IV, Chapter 28.*

[2] Halina Abramowicz et al. The International Linear Collider Technical Design Report - Volume 4: Detectors. 2013, 1306.6329.

[3] C. Adloff et al. Hadronic energy resolution of a highly granular scintillator-steel hadron calorimeter using software compensation techniques. *JINST*, 7:P09017, 2012, 1207.4210.

[4] C. Adloff et al. The Time Structure of Hadronic Showers in highly granular Calorimeters with Tungsten and Steel Absorbers. *JINST*, 9:P07022, 2014, 1404.6454.

[5] S. Agostinelli et al. GEANT4: A Simulation toolkit. *Nucl. Instrum. Meth.*, A506:250–303, 2003.

[6] G. Alexander et al. A Comparison of b and u d s quark jets to gluon jets. *Z. Phys.*, C69:543–560, 1996.

[7] J. B. Birks. *The theory and practice of scintillation counting*. Pergamon Press Oxford, 1964.

[8] Andy Buckley. The hepthesis LaTeX class.

[9] G. Folger and J. P. Wellisch. String parton models in GEANT4. *eConf*, C0303241:MOMT007, 2003, nucl-th/0306007.

[10] F. Gaede. Marlin and LCCD: Software tools for the ILC. *Nucl. Instrum. Meth.*, A559:177–180, 2006.

[11] M. P. Guthrie, R. G. Alsmiller, and H. W. Bertini. Calculation of the capture of negative pions in light elements and comparison with experiments pertaining to cancer radiotherapy. *Nucl. Instrum. Meth.*, 66:29–36, 1968.

[12] Lucie Linssen, Akiya Miyamoto, Marcel Stanitzki, and Harry Weerts. Physics and Detectors at CLIC: CLIC Conceptual Design Report. 2012, 1202.5940.

[13] J. S. Marshall, A. MÃijnnich, and M. A. Thomson. Performance of Particle Flow Calorimetry at CLIC. *Nucl. Instrum. Meth.*, A700:153–162, 2013, 1209.4039.

[14] P. Mora de Freitas and H. Videau. Detector simulation with MOKKA / GEANT4: Present and future. In *Linear colliders. Proceedings, International Workshop on physics and experiments with future electron-positron linear colliders, LCWS 2002, Seogwipo, Jeju Island, Korea, August 26-30, 2002*, pages 623–627, 2002.

[15] C. Patrignani et al. Review of Particle Physics. *Chin. Phys.*, C40(10):100001, 2016.

[16] Torbjorn Sjostrand, Stephen Mrenna, and Peter Z. Skands. PYTHIA 6.4 Physics and Manual. *JHEP*, 05:026, 2006, hep-ph/0603175.

[17] M. A. Thomson. Particle Flow Calorimetry and the PandoraPFA Algorithm. *Nucl. Instrum. Meth.*, A611:25–40, 2009, 0907.3577.

[18] R. Wigmans. Calorimetry: Energy measurement in particle physics. *Int. Ser. Monogr. Phys.*, 107:1–726, 2000.

List of figures

List of tables